AFRL-AFOSR-JP-TR-2018-0015

Development of Large Blue-Phase Liquid Crystal in Single-Crystal Form

Tsung-Hsien Lin
National Sun Yat-Sen University

12/18/2018
Final Report

Air Force Research Laboratory
AF Office Of Scientific Research (AFOSR)/ IOA
Arlington, Virginia 22203
Air Force Materiel Command

REPORT DOCUMENTATION PAGE

Form Approved
OMB No. 0704-0188

1. REPORT DATE *(DD-MM-YYYY)*	2. REPORT TYPE	3. DATES COVERED *(From - To)*
22-02-2018	Final	31 Aug 2015 to 30 Aug 2017

4. TITLE AND SUBTITLE
Development of Large Blue-Phase Liquid Crystal in Single-Crystal Form

5a. CONTRACT NUMBER

5b. GRANT NUMBER
FA2386-15-1-4086

5c. PROGRAM ELEMENT NUMBER
61102F

6. AUTHOR(S)
Tsung-Hsien Lin

5d. PROJECT NUMBER

5e. TASK NUMBER

5f. WORK UNIT NUMBER

7. PERFORMING ORGANIZATION NAME(S) AND ADDRESS(ES)
National Sun Yat-Sen University
70, Lien Hai Rd
Kaohsiung City, 80424 TW

8. PERFORMING ORGANIZATION REPORT NUMBER

9. SPONSORING/MONITORING AGENCY NAME(S) AND ADDRESS(ES)
AOARD
UNIT 45002
APO AP 96338-5002

10. SPONSOR/MONITOR'S ACRONYM(S)
AFRL/AFOSR IOA

11. SPONSOR/MONITOR'S REPORT NUMBER(S)
AFRL-AFOSR-JP-TR-2018-0015

12. DISTRIBUTION/AVAILABILITY STATEMENT
A DISTRIBUTION UNLIMITED: PB Public Release

13. SUPPLEMENTARY NOTES

14. ABSTRACT
The PI had excellent work on this project. The PI reports the fabrication of extraordinarily large monocrystalline photonic crystals by controlling the self-assembly processes which occur in unique phases of liquid crystals that exhibit three-dimensional photonic-crystalline properties called liquid-crystal blue phases. They have also described the a process and technique for growing these crystals. The work has been recently published in the journal Nature Communications in 2018 with AFRL researchers.

15. SUBJECT TERMS
Photonic Crystals, Processing, Optical Properties, Liquid Crystals, Crystal Growth, AOARD

16. SECURITY CLASSIFICATION OF:			17. LIMITATION OF ABSTRACT	18. NUMBER OF PAGES	19a. NAME OF RESPONSIBLE PERSON
a. REPORT	b. ABSTRACT	c. THIS PAGE			CHEN, JERMONT
Unclassified	Unclassified	Unclassified	SAR	16	19b. TELEPHONE NUMBER *(Include area code)* 315-227-7007

Standard Form 298 (Rev. 8/98)
Prescribed by ANSI Std. Z39.18

Final Report for AOARD Grant FA2386-15-1-4086
"Development of large Blue-Phase liquid crystal in single-crystal form"

Date 12/18/2017

PI and Co-PI information:
Tsung-Hsien Lin; jameslin@faculty.nsysu.edu.tw);
National Sun Yat-sen University;
Department of Photonics; 70 Lienhai Rd., Kaohsiung 80424, Taiwan;
+886-5252000#4442.

Period of Performance: 08/31/2015 – 08/30/2017

Abstract: Although there have been intense efforts to fabricate large three-dimensional photonic crystals in order to realize their full potential, the technologies developed so far are still beset with various material processing and cost issues. Conventional top-down fabrications are costly and time-consuming, whereas natural self-assembly and bottom-up fabrications often result in high defect density and limited dimensions. Here we report the fabrication of extraordinarily large monocrystalline photonic crystals by controlling the self-assembly processes which occur in unique phases of liquid crystals that exhibit three-dimensional photonic-crystalline properties called liquid-crystal blue phases. In particular, we have developed a gradient temperature technique that enables three-dimensional photonic crystals to grow to lateral dimensions of ~1 cm (~30,000's of unit cells) and thickness of ~100 μm (~300's of unit cells). These giant single crystals exhibit extraordinarily sharp photonic bandgaps with high reflectivity, long-range periodicity in all dimensions and well-defined lattice orientation. We have also demonstrated that the photonic bandgap of a large polymer-stabilized BP single crystal can be spectrally shifted by ~100 nm in response to small electric fields (~1 V/μm).

Introduction: Most of the findings reported herein is adequately described in Ref. 1 of the List of Publications. Following is the full report of the work modified from our paper published by the journal Nature Communications [1]. Three-dimensional (3D) photonic crystals, an optical analogue of atomic lattices, are attractive materials for versatile manipulation of light.[1–9] In a 3D photonic crystal, the dielectric constant is tailor-made to vary periodically in three dimensions, giving rise to a so-called photonic bandgap which prohibits electromagnetic propagation and substantially modifies the dispersion around a specific wavelength (frequency) region. 3D photonic crystals and their variants that contain specifically designed defect structures to further modify their electromagnetic properties continue to attract intensive interest in the quest to realize efficient dispersion engineering, micro integrated circuits, mirrorless lasers, and other advanced photonic applications. One of the greatest challenges in realizing 3D photonic crystals for application in the optical domain at sub-micrometer wavelengths is the efficient fabrication of large-dimension (> 1000's unit cells) crystals with high refractive index contrast. There have been many attempts to develop large periodic nanostructures including layer-by-layer photolithography, colloidal self-assembly, direct laser writing, and holographic lithography[2,3,6,9,10]. All processes and techniques employed so far are still laden with many technical and/or cost challenges, especially for cases where the photonic crystals are designed to work in the ultraviolet-visible spectrum.

Here we report the experimental realization of a truly 3D photonic crystal built from a unique

phase of liquid crystal, namely blue-phase liquid crystal (BPLC)[11–34]. BPLCs are a special class of chiral nematics (also termed cholesterics) in which the director axes self-assemble into doubly twisted helices and exhibit three phases BPIII, BPII and BPI in order of decreasing temperature from the isotropic liquid phase. BPIII is amorphous, whereas BPII and BPI are simple cubic (SC) and body-centered cubic (BCC), respectively, with lattice constants on the order of a few 100's nm. BPI and BPII thus exhibit selective Bragg reflections in the visible spectrum. Owing to their intrinsic liquid crystal properties, BPLCs are electro-optically active[14,15,20,21,24,25] as well as highly nonlinear[16-19,22,23]. Although BPLCs as photonic crystals have been widely studied, most applications to date employ only polycrystalline or nearly amorphous structures.[18,20,23,24] There have been some attempts to align BP polycrystals by surface treatment or externally applied electric fields[26–29]. Surface alignment, though proven effective in generating monodomain crystals, works only with the BPII phase in thin samples[27–29] (a few microns). Using an applied electric field[26], only the crystallographic axis parallel to the field is guaranteed, whereas the lattice orientations in other dimensions remain random, prohibiting application in many photonic systems where the lateral crystal orientation is also of crucial importance[5,7,8,30] (e.g. preserving the transverse optical wavefront integrity of light). Additionally, randomly distributed lattices tend to degrade the quality factor and increase the scattering loss. According to Belyakov et al.[31], replacing the polycrystal with a single crystal enables the optical rotatory power to be enhanced by almost 40 %. Others have shown that increasing the grain size diminishes the hysteresis during electro-optic switching and reduces the required driving voltage.[32,33] For advanced photonic applications a sufficiently large monocrystalline photonic crystal is therefore highly desirable.

In this work, we developed a gradient temperature technique based on our detailed studies of the self-assembly and re-assembly processes in the ordered Blue Phases. This technique enables the fabrication of monocrystalline photonic crystals of unprecedented dimensions [lateral dimensions of ~1 cm, ~30,000's of unit cells, and thickness of ~100 μm, ~300's of unit cells] by controlling the natural self-assembly processes in blue-phase liquid crystals. Being able to increase the number of periods in a photonic crystal (N) not only extends the interaction length but also greatly improves the optical properties of a photonic crystal such as the photon density of states at the bandedge (proportional to N^2).[35] A significant increase of N from 100 to 10,000 will enhance the density of states by ~10,000 times, impacting group velocity, lasing threshold, spontaneous emission, and optical nonlinearity.[4,36,37] Furthermore, we have also demonstrated the possibility of polymer stabilization that enables not only a much wider operating temperature range of these crystals but also exceptional electrical tunability of their spectral properties. These giant single crystals exhibit extraordinarily sharp photonic bandgaps with high reflectivity, long-range periodicity in all dimensions and well-defined lattice orientation. The colossal, well-oriented BPLCs in either the polymer-free or polymer-stabilized form will serve as excellent templates for more advanced structures and diverse material systems[38–40], as well as topological platforms for molecular self-assembly and symmetry-protected topological photonic crystals[41,42].

Experiment: Four polymer-free and one polymer-stabilized BPLCs were employed in this study: M1, M2, M3, M4, and M5. M1 is a mixture of 44.0 wt% nematic MDA-00-3461 (from Merck), 20.0 wt% nematic 5CB (from HCCH), and 36.0 wt% chiral smectic R811 (from Merck). On cooling from ISO, BPII nuclei appear at 38.5°C, and the ISO coexists with BPII until the temperature decreases to 37.7°C, below which the M1 turns into monophasic BPII. BPI emerges at 36.5°C, and the mono-BPI spans from 36.2°C to 34.6°C, below which the N* comes into sight.

M2 is composed of 32.0 wt% nematic HTW114200-050 (from HCCH), 33.0 wt% 5CB, and 35.0 wt% R811, showing a phase sequence of ISO-(35.6–34.5°C)-BPII-(34.0–33.9°C)-BPI-(29.8°C)-N* on cooling. M3 consists of 35.0 wt% HTW114200-050, 25.0 wt% 5CB, and 40.0 wt% R811, having a similar sequence to M2 on cooling: ISO-(33.4–32.9°C)-BPII-(32.7–32.6°C)-BPI-(28.4°C)-N*. M4 consists of 30.0 wt% HTW114200-050, 37.0 wt% 5CB, and 33.0 wt% R811, exhibiting a phase sequence of ISO-(33.6–32.8°C)-BPII-(32.1–32.0°C)-BPI-(28.1°C)-N*. The precursor of the polymer-stabilized BP, designated as M5, is composed of 54.8 wt% HTW114200-050, 36.5 wt% R811, 4.0 wt% mesogenic cross-linker RM257 (from HCCH), 4.0 wt% 2-ethylhexyl acrylate (from Sigma-Aldrich), and 0.7 wt% photoinitiator Irgacure 651 (from BASF), showing a phase sequence of ISO-(38.1°C)-BPII-(34.5°C)-BPI-(27.0°C)-N*. The precursor was infiltrated into a 12 μm-thick cell and subsequently exposed to ultraviolet light (XLite380, OPAS; centered at $\lambda = 365$ nm) with an intensity of 20 mW cm^{-2} for 60 min to ensure complete polymerization. The PSBP turns from ISO to BPI at ~37.0°C, and it is well stabilized in the BPI even when the ambient temperature plummets to 13.0°C (the lower limit of our experimental condition). The cells are composed of a pair of glass slides with plastic spacers to determine the cell gap: 100 and 300 μm for the polymer-free BPLCs and 12 μm for the polymer-stabilized BPLC demonstrated herein. For samples utilized to perform the experiments shown in Figs. 7–9, the substrates were precoated with polyimide SE-8793 (Nissan) and rubbed with cloth to induce uniform planar alignment.

We demonstrate two methods of growing large BP single crystals: self-reassembly and gradient-temperature scanning (GTS). In the self-reassembly approach, we hold the samples at the BPII letting the small platelets gradually self-reassemble into mm-size monocrystals. A temperature control system, mK2000, was implemented. In Fig. 1, we summarize the effect of holding temperature on the crystal growth. M1 was cooled from ISO with a rate of 10°C min^{-1} to a specified temperature shown on the horizontal axis, and subsequently sit for 3 hours before measurement shown in Fig. 1a. For Fig. 1b,c, the holding temperatures were set at 36.6°C for BPII and 36.0°C for BPI. Upon quenching from the isotropic phase to a single blue phase or a mixed phase, abundant BP platelets nucleated in the isotropic melt. Before these nuclei grew large, the process was terminated by meeting others (in just a few seconds upon reaching the set temperature). Subsequently, the self-reassembly (platelet-merger) process was initiated. The speed of self-reassembly varies dramatically with the set phase (cf. Fig. 1). The growth process demonstrated in Fig. 2 —successive quenching— was accomplished by the following steps. Step 1: Quenching the sample from the ISO to the BPII (36.6°C) at a rate of 10°C min^{-1}. Step 2: Holding the sample at 36.6°C (mono-BPII) for 36 hours to let the BPII crystals grow spontaneously by platelet merger. Step 3: Using the grown single crystals of BPII as seeds to form large BPI crystals via quenching from the BPII to the BPI (36.2°C) at a rate of 10°C min^{-1}. Step 4: Holding the sample for another 24 hours to let the striations anneal out, releasing the mechanical stress generated during the pseudomorphism process (i.e. Step 3). The data in Fig. 2e,f were collected at 36.0°C.

The GTS experiments were conducted using a temperature-controlled enclosure GS350 (Linkam) and controller T95 (Linkam). For the greenish-colored BPI displayed in Figs. 5, 7, and 8, M2 was used, the two temperature-controlled stages were set at 34.5 and 33.0°C, respectively, and the scan rates were 0.02 μm s^{-1} for Fig. 5 and 0.10 μm s^{-1} for Figs. 7 and 8. For the bluish-colored BPI displayed in Fig. 8, M3 was used, the stages were set at 32.8 and 32.4°C, respectively, and the scan rate was 0.10 μm s^{-1}. For reddish-colored BPI shown in Fig. 8, M4 was used, the stages were set at 32.8 and 31.2°C, respectively, and the scan rate was 0.10 μm s^{-1}.

In the experiments, the reflection and transmission spectra were taken using a spectrometer

USB4000 (Ocean Optics). Microscopic images/videos and Kössel diagrams were captured using a charge-coupled device DS-Fi1 (Nikon) that was linked to a polarizing optical microscope Eclipse LV100 POL (Nikon) containing a switchable Bertrand lens. In the Kössel diffraction examination, a 440 nm light with a bandwidth of 10 nm was employed as a light source. The Kössel rings were observed in the back focal plane of the objective. Macroscopic images and video were taken using digital single-lens reflex camera D7000 (Nikon) equipped with lens AF-S VR Micro-Nikkor 105mm f/2.8G IF-ED (Nikon).

For the bandwidth estimation, Yoshida *et al.*'s simulation results[45] suggest that the reflection bandwidth of a BPI crystal ($\Delta\lambda_{BPI}$) is approximately one-fifth of that of a planar cholesteric liquid crystal ($\Delta\lambda_{N*}$), on the assumption that the lattice spacings and material parameters are the same for both; more precisely, $\Delta\lambda_{BPI} = 0.228 \times \Delta\lambda_{N*}$. Therefore, we estimate the bandwidth of a single BPI crystal as follows: (i) Infiltrate the BPLC mixture into a surface-treated sandwich cell at a temperature above the clearing point, followed by cooling of the sample to the cholesteric phase. (ii) Store the sample at 25°C for almost a month to let the planar domains grow. (iii) Capture the transmission spectrum of a planar cholesteric domain. (iv) The bandwidth of a BPI crystal is estimated by substituting $\Delta\lambda_{N*}$ with the measured bandwidth in:

$$\Delta\lambda_{\mathrm{BPI}} = 0.228\times\Delta\lambda_{\mathrm{N^*}}\frac{d_{hkl}}{p} = 0.228\times\Delta\lambda_{\mathrm{N^*}}\frac{\left(\lambda_{\mathrm{c}}/n_{\mathrm{avg}}\right)_{\mathrm{BPI}}}{\left(\lambda_{\mathrm{c}}/n_{\mathrm{avg}}\right)_{\mathrm{N^*}}}, \tag{1}$$

where d_{hkl} is the lattice spacing along the [*h k l*] axis in BPI, p is the helical pitch in N*, λ_c is the center wavelength of the reflection band, and n_{avg} is the average refractive index along the propagation axis. For simplicity, by neglecting the difference between the average indices of BPI (square root of $(n_e^2+ 2n_o^2)/3$) and N* (square root of $(n_e^2+ n_o^2)/2$), Eq. (1) becomes:

$$\Delta\lambda_{\mathrm{BPI}} \cong 0.228\times\Delta\lambda_{\mathrm{N^*}}\frac{\lambda_{\mathrm{c,BPI}}}{\lambda_{\mathrm{c,N^*}}}. \tag{2}$$

Results and Discussion: The results are categorized into three subsections: (i) Self-reassembly and merger of blue-phase platelets, (ii) crystal growth by gradient-temperature scanning, (iii) polymer-stabilized blue-phase single crystal.

(i) Self-reassembly and merger of blue-phase platelets

To gain insight into the self-assembly and reassembly processes of BPLC, a 100 μm-thick cell containing M1 placed in a temperature-controlled enclosure was first cooled from ISO phase at a rapid rate of 10°C min^{-1} to and held (quenched) at a specified temperature for 3 hours before measurement (cf. Experiment section); the temperature/phase dependence of the average grain size obtained is shown in Fig. 1a. In the monophasic-BPII regime (abbreviated to mono-BPII; 37.7–36.5°C), the platelets grew to ~80 μm (in lateral size) on average, with some of them as wide as 120 μm. The grain size dropped dramatically if the holding temperature departs from the mono-BPII phase to ~10 μm in mono-BPI (36.2–34.6°C) phase. In order to gain more insights into the inner working of the growth process, the temporal evolutions of these BPII and BPI platelets, cf. Fig. 1b,c were studied. Upon rapid cooling from the ISO to BPII, the molecules self-assembled into small platelets of ~15 μm in diameter which then underwent multiple reassembly processes. The crystallographic axes of some platelets reoriented to accommodate their contiguous grains with elimination of the grain boundaries. After ~13 hours of such repeated reassembly, the BPII platelets grew gradually to ~300 μm. By contrast, similar

procedures barely yield improvement in the crystalline sizes grown from BPI platelets, similar to other studies employing surface alignment and slow cooling. The difficulty in growing large crystal from the BPI phase compared to BPII is attributable to the fact that within a lattice, all the line defects of BPII intersect with each other thus effectively acting as a single defect, whereas within the BPI phase, the line defects exist independently of one another[27,43] (cf. the insets of Fig. 1b). The platelet-merger phenomenon follows the system's tendency to minimize free energy. When the lattice contains a sole defect (BPII), only one minimum of free energy exists, at which a single crystal is formed. In the case of BPI, there exist numerous defects in one lattice which correspond to many local free energy minima. This study implies that, a large single crystal can be grown only in the monophasic BPII temperature interval, cf. Fig. 1a. Such a platelet reassembly process involves the crystallographic-axis reorientation of an entire crystal; as the BPII platelets grows larger, the required energy for lattice rearrangement becomes larger until a local equilibrium occurs as indicated in Fig. 1b. We observed that several large BPII monocrystals of ~1 mm in lateral size can be obtained after the sample has sat for one week.

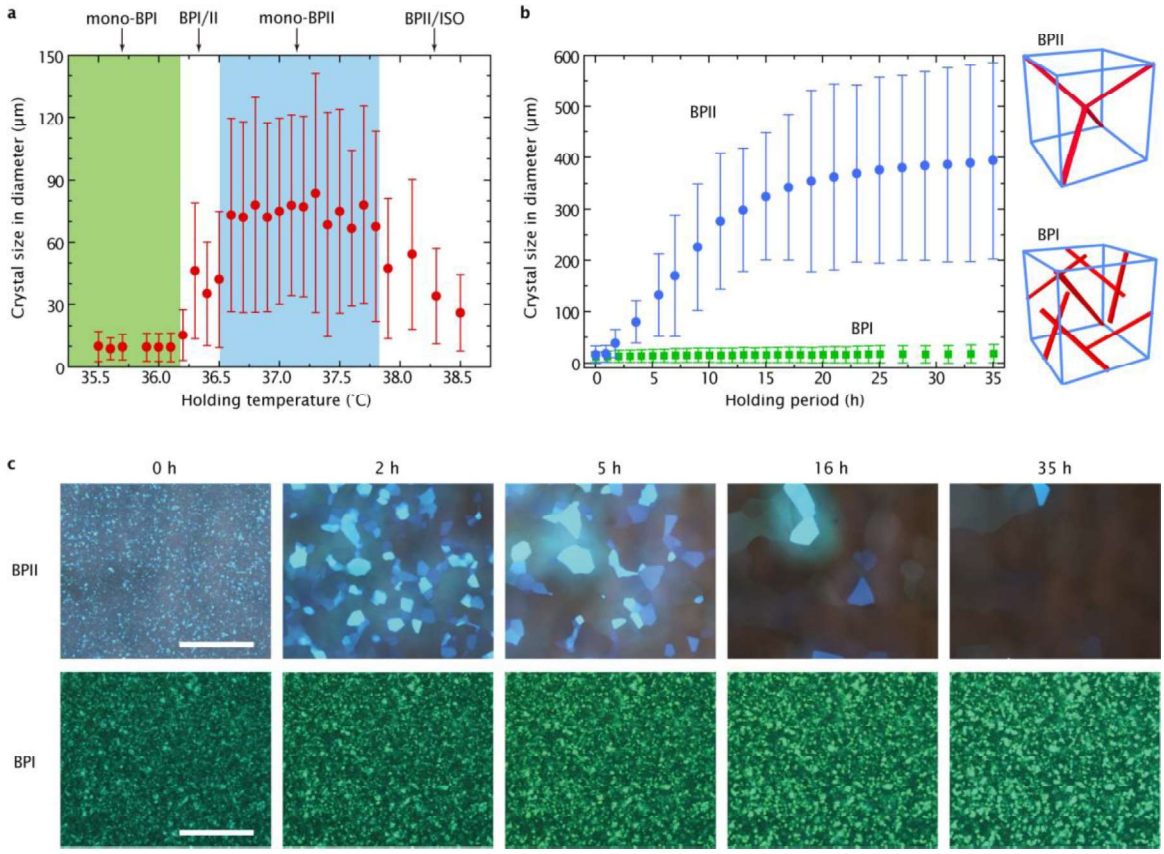

Figure 1 | Self-reassembly of a BPLC. a, Crystal size of BPLC M1 as a function of holding temperature/phase, measured after holding the sample at the respective temperatures for three hours upon cooling from the ISO phase. **b,** Sizes of BPII and BPI monocrystals as a function of holding time; the insets show the defect structures in unit cells of BPII and BPI, respectively. The data points for Fig. 1a,b were obtained by averaging the areal size of all platelets within the field of view; error bar indicates the deviation from the average size. Each platelet is approximated by an enclosing circle of diameter. **c,** Microscope images of BPII and BPI crystals as a function of time (scale bars, 500 μm). See section 'Experiment' for experimental details.

We have then discovered that using a well-formed BPII crystal as a precursor/mold it is possible to grow BPI single crystals of record-setting sizes. The capability to fabricate massive-sized BPI as well as BPII single crystals is important as it provides more choices of lattice structures (e.g. BCC structure, and various non-cubic lattice structures of electrically

distorted BPI[25]) and wider temperature ranges[11,12]. Some important features of the growth process in the BPI phase are depicted in Fig. 2a–d (see section 'Experiment' for more details on the successive quenching process). Figure 2b,c reveals that the contour of BPII platelets was completely preserved upon rapid annealing to BPI. Such pseudomorphic transformation commenced with the formation of striations in two directions generated from the mismatch between the two lattice structures[44]. These striped patterns also provide further information on the lattice orientation. By applying the Kössel diffraction technique to identify the lattice orientation, the bisector of the obtuse angle formed by the striations was identified as nearly matching the [200] axis of the BPI crystal (Fig. 3). Large and uniform BPI single crystals were formed with high reflectivity and narrow bandwidth. Figure 2e,f also clearly indicates that over a wide field of view-area (~1 mm^2), the reflection bandwidth of such an extreme-sized photonic monocrystal was found to be dramatically narrower than that of a commonly used BP polycrystal—~11 nm as opposed to ~83 nm, approaching the theoretical expectation[45] (cf. Experiment). Furthermore, a nearly millimeter^2-sized BPI monocrystal (area $A \approx 0.9$ mm^2; thickness $d \approx 100$ μm) shown in Fig. 4 greatly exceeds the previously held record of $A \approx 0.2$ mm^2 with $d \approx 6$ μm[34]. As observed under a polarizing optical microscope (Fig. 4), the terraces[3] become more closely spaced and the reflectivity drops near the convergent grain boundary (e.g., from (1) to (2) and from (1) through (3) to (4)). The corresponding Kössel diagrams also imply the occurrence of macroscopic lattice deformation near the grain boundary; more precisely, a gradual inclination of the ⟨011⟩ axis towards the boundary. As for (5) and (6), the Kössel patterns indicate that they belong to an identical crystal with the orientation different from the neighboring (orange) ones.

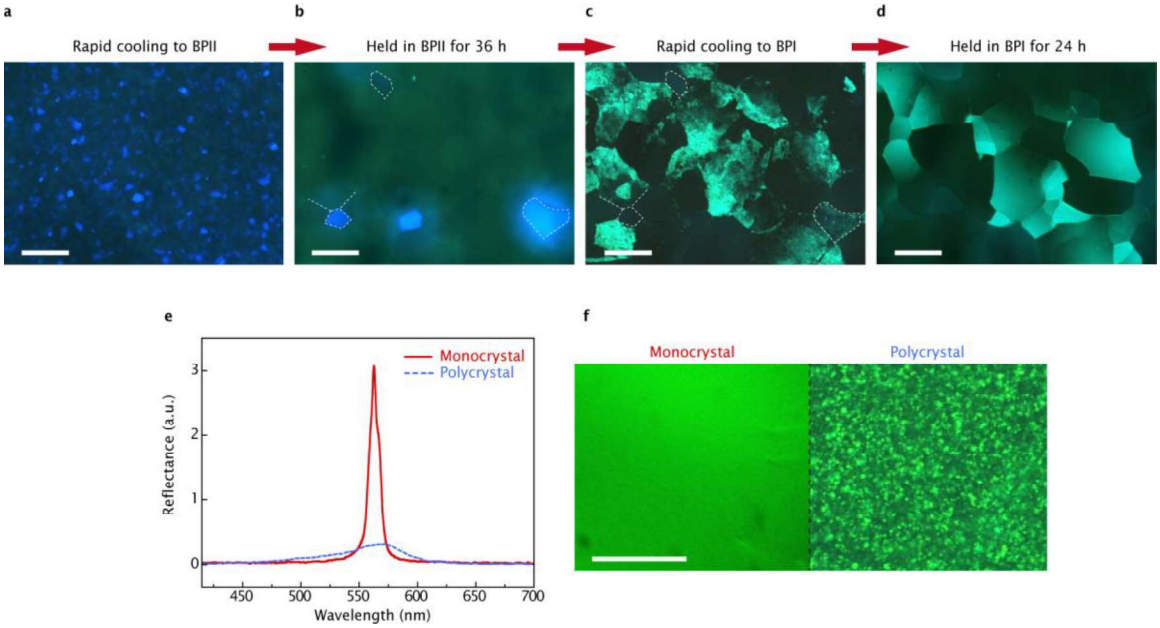

Figure 2 | Formation of large BPI single crystals by self-reassembly and pseudomorphism. Formation process: microscopic images of M1 **a,** upon cooling to BPII from ISO → **b,** upon holding for 36 hours in BPII → **c,** upon cooling to BPI → **d,** upon holding for 24 hours in BPI (scale bars, 300 μm). Optical characterization of BPI monocrystal and polycrystal: **e,** reflection spectra and **f,** microscope images (scale bar, 100 μm). See section 'Experiment' for experimental details.

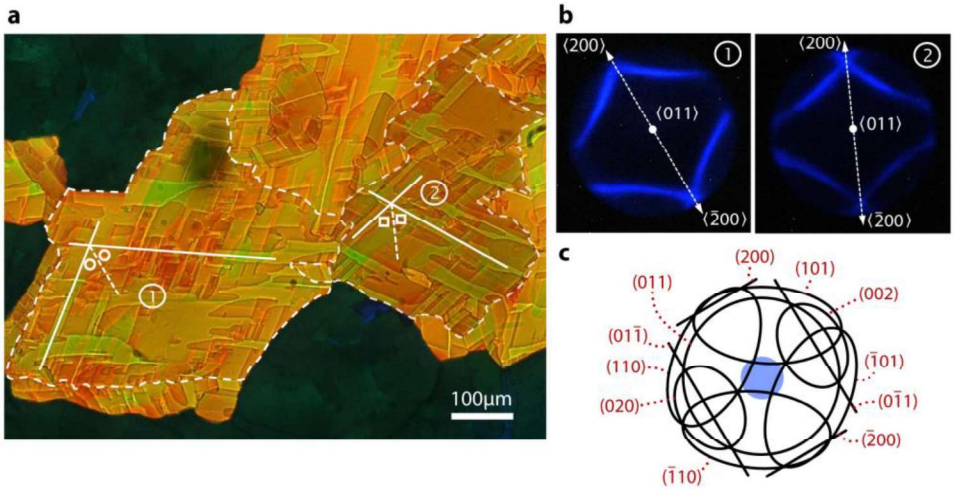

Figure 3 | Correlation between crosshatching and lattice orientation. **a**, Microscope image of a few sub-mm-sized BPI crystals captured upon direct cooling from BPII. **b**, Observed Kössel diagrams for crystals (1) and (2). **c**, Theoretical Kössel diagram for a BPI crystal viewed from ⟨011⟩. The blue region describes approximately the field of view of our experimental setup.

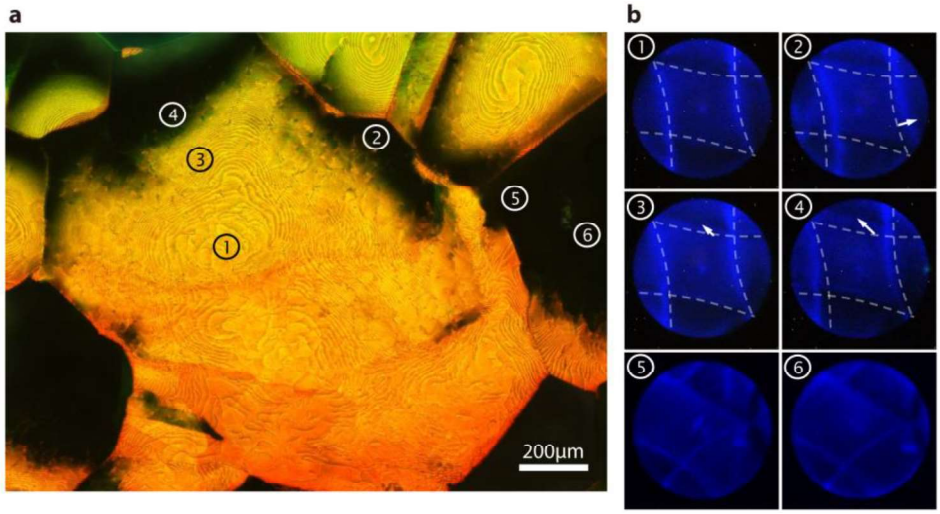

Figure 4 | ~ 1 mm^2-sized BPI monocrystal by self-reassembly in BPII & pseudomorphic transformation to BPI. **a**, Microscope image of the crystal. **b**, Kössel diagrams captured at labeled regions in **a**. The white dashed lines represent the Kössel diffraction pattern of (1).

(ii) Crystal growth by gradient-temperature scanning

In the GTS technique, a spatial gradient of temperature was introduced in the conventional slow-cooling method. The GTS process utilizes the earlier-formed BPI platelets as seeds/nuclei for crystal growth. The system consists of a chamber enclosing a step motor and two temperature-controlled stages with a gap of ~2 mm in between (Fig. 5a). One of the heating stages is set at a temperature in the mono-BPII regime (designated as the high-$\boldsymbol{T}$ stage), while the other is situated at a mono-BPI temperature (designated as the low-$\boldsymbol{T}$ stage). Placing the cell across the two stages generates a gentle gradient of temperature. A micrometer step motor is used to move the sample from one stage to the other ensuring a controllable shift of the temperature gradient. Figure 5b displays an approximately 3 mm BPI monocrystal in a M2 cell ($d \approx 100$ μm) grown by this technique with a scan rate of ~0.02 μm s^{-1}. A continuous color

variation from blue-green to green reveals the spatial temperature gradient from high to low temperature.

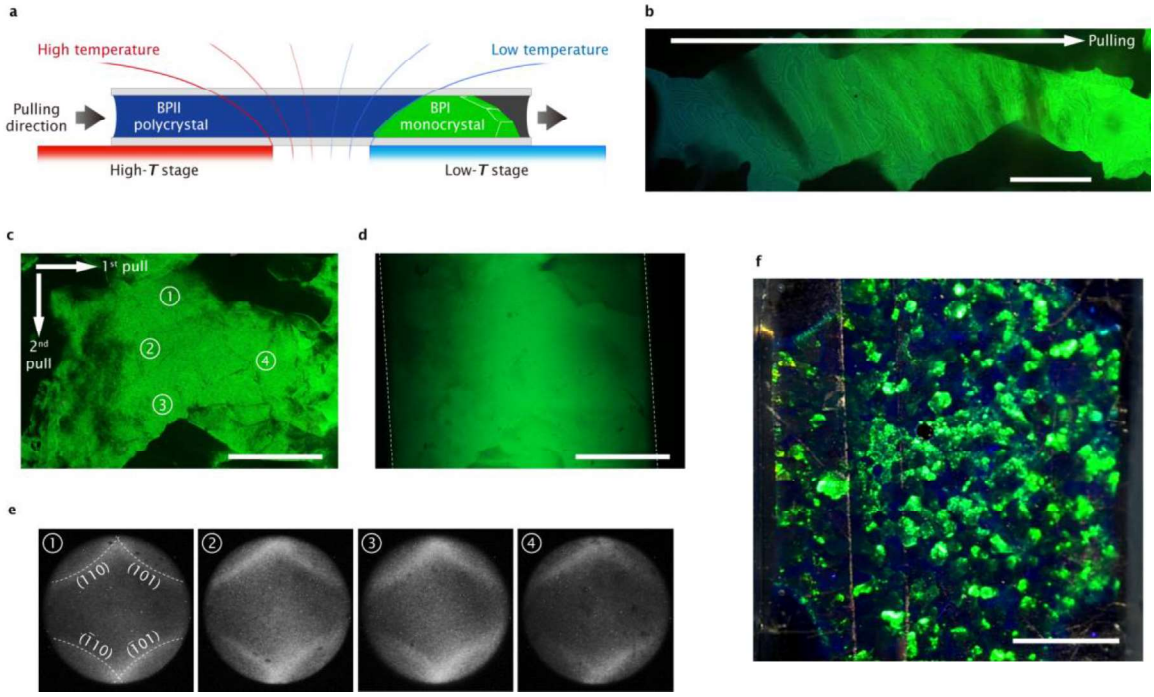

Figure 5 | Formation of large BPI single crystals by gradient-temperature scanning. a, Schematic depiction of the GTS system. **b,** Microscope image of a 3 mm-long BPI single crystal fabricated by 1D GTS (reflection; scale bar, 500 μm). Microscope images of a 1.2×0.7×0.3 mm^3-sized BPI monocrystal by 2D GTS in the **c,** reflection and **d,** transmission modes, respectively (scale bars, 500 μm). **e**, Kössel diagrams captured at different labeled regions of the single crystal. **f,** Macroscopic view of the sample with mm-sized BPI monocrystals (reflection; scale bar, 3 mm).

To achieve large crystal sizes in two dimensions and avoid unexpected growth termination by ambient temperature fluctuations, a "melt-and-regrow" strategy was devised, cf. Fig. 6. By reversing the pulling direction, the grain boundaries of the BPI monocrystals can be erased, i.e., melted to BPII (Fig. 6a,b). The growth process can subsequently be reactivated by reversing the pulling direction again (Fig. 6c). After growing to the desirable extent in one dimension (say $\boldsymbol{x}$), the cell was rotated by 90°; one of the long edges of the grown BPI monocrystal was then melted (transitioned to the BPII phase) and allowed to grow in the other direction ($\boldsymbol{y}$). In this manner, a 1200×700 μm^2-area and 300 μm thick single BPI crystal was successfully grown, and it exhibits spectacular reflection and transmission properties as shown in Fig. 5c,d. The image taken in the transmission mode indicates a continuous lattice along the longitudinal axis of the cell. The Kössel diffraction technique was used to confirm the unity of lattice orientation within the platelet (Fig. 5e). Figure 5f shows a macroscopic view of a cell containing millimeter-sized BPI monocrystals.

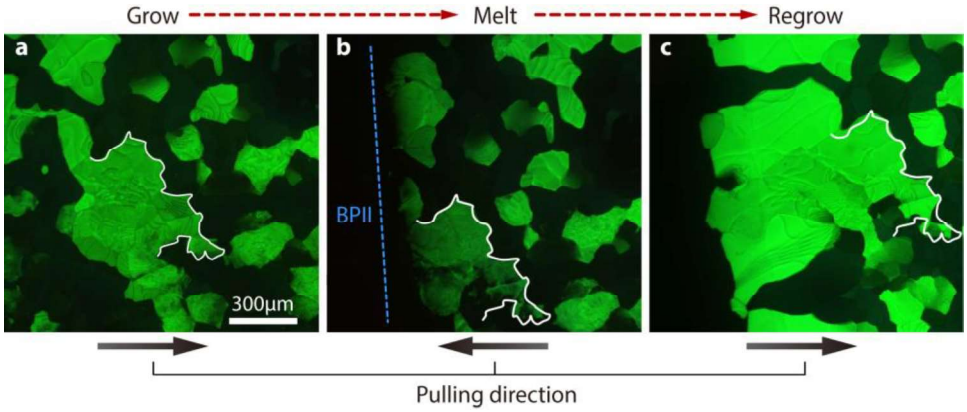

Figure 6 | Melt and regrow. a, BPI monocrystals grown with a scan rate of 0.05 μm s^{-1}. The white solid line outlines part of a monocrystal for comparison with **b** & **c**. **b**, The grain boundaries of the BPI monocrystals are melt into BPII. The blue dotted line vaguely defines the interface of BPII and BPI. **c**, BPI monocrystals with extended length, regrown using a scan rate of 0.02 μm s^{-1}.

To improve the uniformity of the grown BPI monocrystals, predetermination of lattice orientation is required and it is realized by treating the substrate with a rubbed polyimide layer. As illustrated in Fig. 5a, the temperature gradient exists not only in the scanning direction but also in the third (longitudinal) dimension, thereby influencing the nucleation of BPI to take place on the surface instead of the bulk. This enables the alignment layer to orient the nuclei effectively. Using this technique, a perfectly oriented, nearly flat, ~10×5×0.1 mm^3-sized BPI monocrystal was grown. Figure 7a shows a crystal on the low-$\boldsymbol{T}$ stage (monodomain BPI), a variant across the temperature gap (BPI to BPII crystal), and a deep-blue crystal in high-$\boldsymbol{T}$ stage region (BPII). Three regions of this large BPI crystal were randomly selected and microscope images (Fig. 7b) and Kössel diagrams (Fig. 7c) were captured. The number of terraces are significantly reduced and the Kössel diagrams are nearly identical, confirming the uniformity of the crystal (cf. Figs. 4 and 5). The diffraction patterns also indicate that the grown crystal is arranged with its ⟨011⟩ direction parallel to the viewing axis and ⟨200⟩ direction placed at a small angle to the rubbing direction $\boldsymbol{R}$ (cf. Fig. 7d). Figure 4e plots the transmission and reflection spectra of one of the selected regions. The sharp transmission dip with a bandwidth of ~13 nm observed across a lateral extent of ~500 μm [and a longitudinal dimension of 100 μm that is equivalent to ~300 unit cells] indicates the uniformity of the monocrystal on the plane parallel to the substrate. It is noteworthy that the bandwidth of the transmission dip is in good agreement with theoretical estimate (cf. Experiment). It is important to note that even though the samples have been treated with surface alignment, without GTS, the BPI crystals grown by homogeneously annealing from BPII or ISO will be polycrystalline and randomly oriented, especially for thick cells (cf. Fig. 7f and Ref. 27). Additionally, with the aid of surface alignment, the GTS enables a higher growth rate of 0.1 μm s^{-1} (compared to 0.02 μm s^{-1} as mentioned previously).

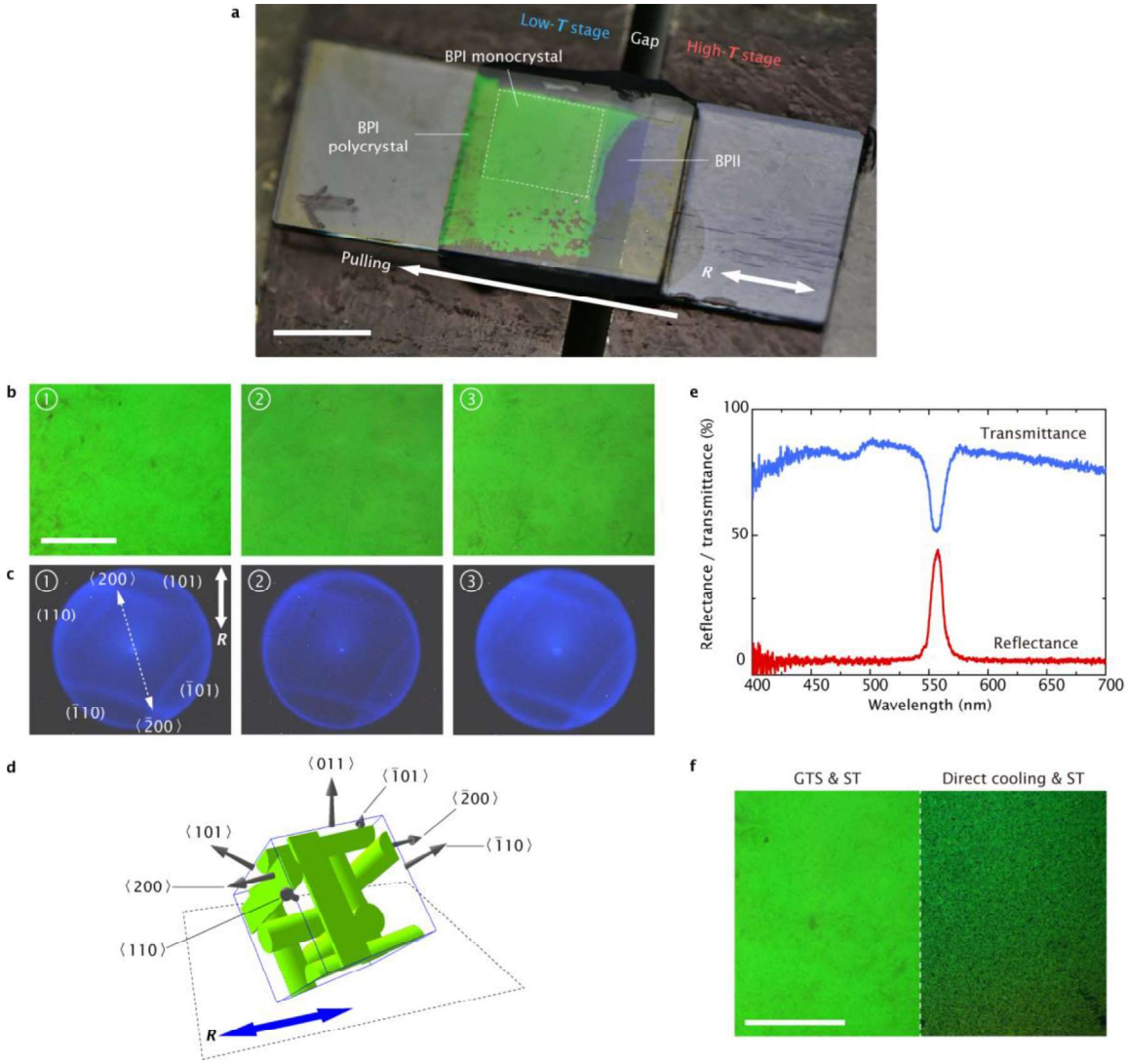

Figure 7 | Surface treatment-assisted gradient-temperature scanning growth. a, Macroscopic view of a 100 μm-thick M2 sample during GTS (scale bar, 5 mm). **b,** Microscope images at different parts of the grown monocrystal (scale bar, 500 μm) and **c,** respective Kössel diagrams. **d,** Schematic depiction of the crystal orientation relative to alignment axis (***R***). **e,** Transmission and reflection spectra of the single crystal. Note: the absence of a Darwin plateau at the peak reflection (or transmission dip) observed in their 1D counterpart (cholesteric liquid crystal) is simply due to the very small index difference in the BPLC unit cells compared to the index modulation in the cholesteric liquid crystal. **f,** A set of microscope images comparing BPI crystals in the surface-treated (ST) sample grown by GTS (left; scale bar, 500 μm) and direct cooling (right).

Here three mm^2-sized and ~mm-thick BPI monocrystals with red, green, and blue reflections were prepared by the surface-alignment assisted GTS process (Fig. 8a,b) to demonstrate that BPLCs as a 3D photonic crystal platform can adapt to different spectral regimes across the visible spectrum. All three monocrystals are composed of the same constituents but having different mixing ratios (see section 'Experiment' for more details). A blue-shift of the photonic bandgap is accomplished by increasing the concentration of the chiral agent. Figure 5b reveals that, without any anti-reflective coating, the photonic bandgap of each single crystal has a bandwidth of ~10–14 nm and reflectance of over 45 %, almost reaching the theoretical maximum of reflection for a linearly polarized input.

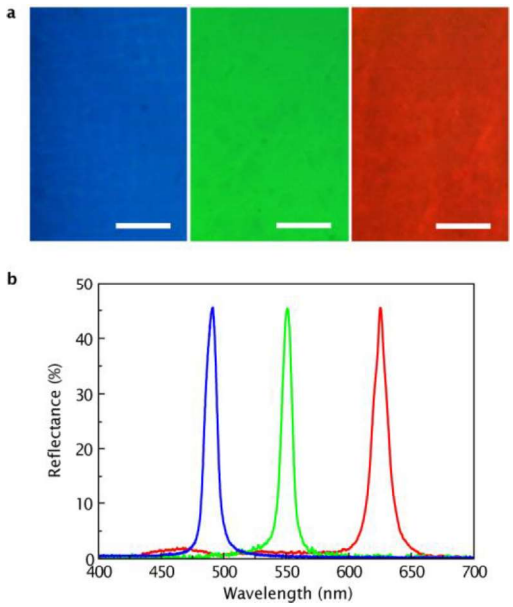

Figure 8 | Blue, green, and red reflections from large BP single crystals. a, Microscope images of three different BPI single crystals (scale bars, 200 μm) and **b,** respective reflection spectra for linearly polarized probe light. See section 'Experiment' for fabrication details.

(iii) Polymer-stabilized blue-phase single crystal

By adding a polymer scaffold *in-situ* through photopolymerization will thermodynamically stabilize a BPLC by templating the underlying lattice structure. Figure 6a demonstrates that these large monodomain BP crystals can also be so stabilized and do indeed exhibit a much wider temperature range (at least 25°C) compared to their polymer-free counterparts (typically ~1–4°C); temperature sensitivity of the photonic bandgap has also been suppressed, measuring $d\lambda/dT \approx 0.16$ nm °C^{-1}. The polymer-stabilized monocrystal possesses excellent dynamic tunability over a wide color range under direct current electric fields caused by field-induced distortion of the polymeric lattice scaffold[21]. Figure 9 reveals that the photonic bandgap can be linearly shifted with increasing field (~88 nm per V μm^{-1} above the threshold at ~0.15 V μm^{-1}) from green to red. A dynamic tuning range of over 100 nm has been achieved with only ~1.3 V μm^{-1}. The lattice distortion is fully reversible, and the hysteresis between increasing and decreasing field strength is almost negligible. The success in polymer-stabilizing a single BP crystal of such extraordinary size not only removes concerns regarding the narrow temperature range of BP but also clearly indicates the feasibility of BP-templated fabrication to yield flexible photonic-crystal gel systems[16,20].

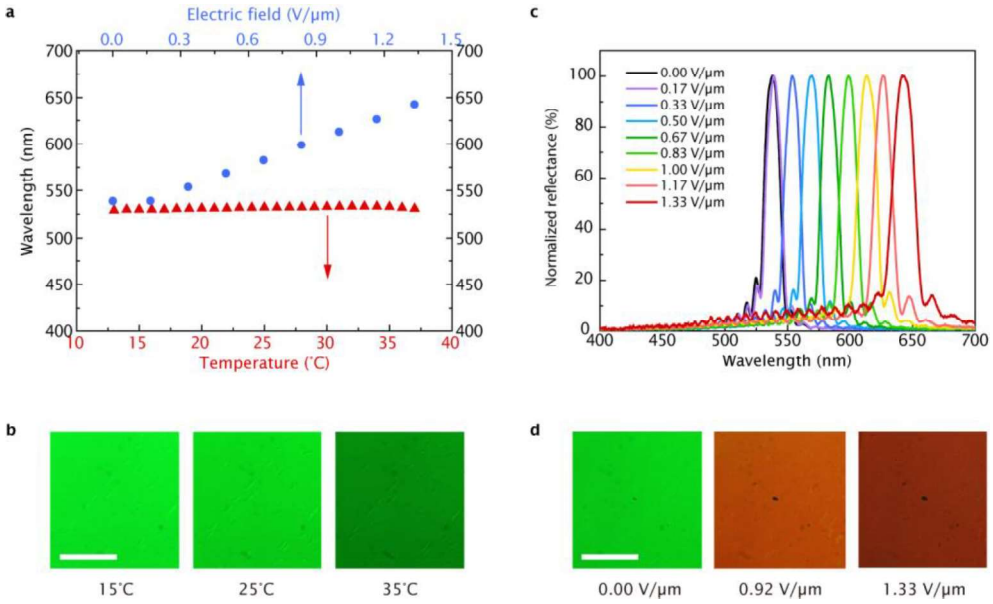

Figure 9 | Temperature-invariant and electrically tunable photonic bandgap of large polymer-stabilized BP monocrystal. a, Temperature and electric field dependences of the peak reflection wavelength. **b,** Microscope images at different temperatures (scale bar, 500 μm). **c,** Reflection spectra at different direct-current field strengths. **d,** Microscope images at different field strengths (scale bar, 500 μm).

References:

1. Joannopoulos, J. D., Villeneuve, P. R. & Fan, S. Photonic crystals: putting a new twist on light. *Nature* **386**, 143-149 (1997).
2. Blanco, A. *et al.* Large-scale synthesis of a silicon photonic crystal with a complete three-dimensional bandgap near 1.5 micrometres. *Nature* **405**, 437-440 (2000).
3. Arsenault, A. *et al.* Towards the synthetic all-optical computer: science fiction or reality? *J. Mater. Chem.* **14**, 781-794 (2004).
4. SoljaCiC, M. & Joannopoulos, J. D. Enhancement of nonlinear effects using photonic crystals. *Nature Mater.* **3**, 211-219 (2004).
5. Rinne, S. A., Garcia-Santamaria, F. & Braun, P. V. Embedded cavities and waveguides in three-dimensional silicon photonic crystals. *Nature Photon.* **2**, 52-56 (2008).
6. von Freymann, G. *et al.* Three-Dimensional Nanostructures for Photonics. *Adv. Funct. Mater.* **20**, 1038-1052 (2010).
7. Tandaechanurat, A. *et al.* Lasing oscillation in a three-dimensional photonic crystal nanocavity with a complete bandgap. *Nature Photon.* **5**, 91-94 (2011).
8. Turner, M. D. *et al.* Miniature chiral beamsplitter based on gyroid photonic crystals. *Nature Photon.* **7**, 801-805 (2013).
9. Montelongo, Y., Yetisen, A. K., Butt, H. & Yun, S.-H. Reconfigurable optical assembly of nanostructures. *Nature Comm.* **7**, 12002 (2016).
10. Jang, J. H. *et al.* 3D Micro- and Nanostructures via Interference Lithography. *Adv. Funct. Mater.* **17**, 3027-3041 (2007).
11. Wright, D. & Mermin, N. Crystalline liquids: the blue phases. *Rev. Mod. Phys.* **61**, 385-432 (1989).
12. Kitzerow, H. S. Blue phases come of age: a review. *Proc. SPIE* **7232**, 723205 (2009).
13. Yang, D.-K. & Wu, S.-T. in *Fundamentals of Liquid Crystal Devices.* Ch. 13 (John Wiley & Sons, Ltd, 2014).

14. Kikuchi, H., Yokota, M., Hisakado, Y., Yang, H. & Kajiyama, T. Polymer-stabilized liquid crystal blue phases. *Nature Mater.* **1**, 64-68 (2002).
15. Coles, H. J. & Pivnenko, M. N. Liquid crystal 'blue phases' with a wide temperature range. *Nature* **436**, 997-1000 (2005).
16. Castles, F. *et al.* Blue-phase templated fabrication of three-dimensional nanostructures for photonic applications. *Nature Mater.* **11**, 599-603 (2012).
17. Lin, T.-H. *et al.* Red, Green and Blue Reflections Enabled in an Optically Tunable Self-Organized 3D Cubic Nanostructured Thin Film. *Adv. Mater.* **25**, 5050-5054 (2013).
18. Hur, S.-T. *et al.* Liquid-Crystalline Blue Phase Laser with Widely Tunable Wavelength. *Adv. Mater.* **25**, 3002-3006 (2013).
19. Khoo, I. C., Hong, K. L., Zhao, S., Ma, D. & Lin, T.-H. Blue-phase liquid crystal cored optical fiber array with photonic bandgaps and nonlinear transmission properties. *Opt. Express* **21**, 4319-4327 (2013).
20. Castles, F. *et al.* Stretchable liquid-crystal blue-phase gels. *Nature Mater.* **13**, 817-821 (2014).
21. Chen, C.-W. *et al.* Electric Field-Driven Shifting and Expansion of Photonic Band Gaps in 3D Liquid Photonic Crystals. *ACS Photon.* **2**, 1524-1531 (2015).
22. Khoo, I. C., Chen, C.-W. & Ho, T.-J. High efficiency holographic Bragg grating with optically prolonged memory. *Sci. Rep.* **6**, 36148 (2016).
23. Cao, W., Munoz, A., Palffy-Muhoray, P. & Taheri, B. Lasing in a three-dimensional photonic crystal of the liquid crystal blue phase II. *Nature Mater.* **1**, 111-113 (2002).
24. Chen, Y. & Wu, S.-T. Recent advances on polymer-stabilized blue phase liquid crystal materials and devices. *J. Appl. Polym. Sci.* **131** (2014).
25. Kitzerow, H. S. The Effect of Electric Fields on Blue Phases. *Mol. Cryst. Liq. Cryst.* **202**, 51-83 (1991).
26. Chen, Y. & Wu, S.-T. Electric field-induced monodomain blue phase liquid crystals. *Appl. Phys. Lett.* **102**, 171110 (2013).
27. Tanaka, S. *et al.* Double-twist cylinders in liquid crystalline cholesteric blue phases observed by transmission electron microscopy. *Sci. Rep.* **5**, 16180 (2015).
28. Kim, K. *et al.* A well-aligned simple cubic blue phase for a liquid crystal laser. *J. Mater. Chem. C* **3**, 5383–5388 (2015).
29. Jo, S.-Y. *et al.* Polymer Stabilization of Liquid-Crystal Blue Phase II toward Photonic Crystals. *ACS Appl. Mater. Interfaces* **9**, 8941-8947 (2017).
30. Kobashi, J., Yoshida, H. & Ozaki., M. Planar optics with patterned chiral liquid crystals. *Nature Photon.* **10**, 389–392 (2016).
31. Belyakov, V., Demikhov, E., Dmitrienko, V. & Dolganov, V. Optical activity, transmission spectra, and structure of blue phases of liquid crystals. *Zh. Eksp. Teor. Fiz.* **89**, 2035-2051 (1985).
32. Nayek, P. *et al.* Effect of the grain size on hysteresis of liquid-crystalline Blue Phase I. *J. Soc. Inf. Display* **20**, 318-325 (2012).
33. Chen, H.-S., Lin, Y.-H., Wu, C.-H., Chen, M. & Hsu, H.-K. Hysteresis-free polymer-stabilized blue phase liquid crystals using thermal recycles. *Opt. Mater. Express* **2**, 1149-1155 (2012).
34. Onusseit, H. & Stegemeyer, H. Liquid Single Crystals of Cholesteric Blue Phases. *Z. Naturforsch. A* **36**, 1083-1085 (1981).
35. Bendickson, J. M., Dowling, J. P., & Scalora, M. Analytic expressions for the electromagnetic mode density in finite, one-dimensional, photonic band-gap structures. *Phys. Rev. E*, **53**, 4107 (1996).

36. Kogelnik, H., & Shank, C. V. Coupled-wave theory of distributed feedback lasers. *J. Appl. Phys.* **43**, 2327-2335 (1972).
37. Baba, T. Slow light in photonic crystals. *Nature photon.* **2**, 465 (2008).
38. Ravnik, M., Alexander, G. P., Yeomans, J. M. & Žumer, S. Three-dimensional colloidal crystals in liquid crystalline blue phases. *Proc. Natl. Acad. Sci. U.S.A.* **108**, 5188-5192 (2011).
39. Shi, Y., Mo, J., Wei, J. & Guo, J. Chiral assembly and plasmonic response of silver nanoparticles in a three-dimensional blue-phase nanostructure template. *New J. Chem.* **39**, 1899-1904 (2015).
40. H. Yoshida, K. Asakura, J. Fukuda & M. Ozaki, Three-dimensional positioning and control of colloidal objects utilizing engineered liquid crystalline defect networks. Nature Comm. **6**, 7180 (2015).
41. Wang, X., Miller, D. S., Bukusoglu, E., de Pablo, J. J. & Abbott, N. L. Topological defects in liquid crystals as templates for molecular self-assembly. *Nature Mater.* **15**, 106-112 (2016).
42. Lu, L. *et al.* Symmetry-protected topological photonic crystal in three dimensions. *Nature Phys.* **12**, 337-340 (2016).
43. Tiribocchi, A., Gonnella, G., Marenduzzo, D. & Orlandini, E. Switching dynamics in cholesteric blue phases. *Soft Matter* **7**, 3295-3306 (2011).
44. Stegemeyer, H., Blümel, T. H., Hiltrop, K., Onusseit, H. & Porsch, F. Thermodynamic, structural and morphological studies on liquid-crystalline blue phases. *Liq. Cryst.* **1**, 3-28 (1986).
45. Yoshida, H. *et al.* Bragg reflection band width and optical rotatory dispersion of cubic blue-phase liquid crystals. *Phys. Rev. E* **94**, 042703 (2016).

List of Publications and Significant Collaborations that resulted from your AOARD supported project: In standard format showing authors, title, journal, issue, pages, and date, for each category list the following:

[1] C.-W. Chen, C.-T. Hou, C.-C. Li, H.-C. Jau, C.-T. Wang, C.-L. Hong, D.-Y. Guo, C.-Y. Wang, S.-P. Chiang, T. J Bunning, I.-C. Khoo, and T.-H. Lin, "Large three-dimensional photonic crystals based on monocrystalline liquid crystal blue phases," Nat. Commun. **8**, 727 (2017).

[2] T.-H. Lin, C.-W. Chen, C.-L. Hong, H.-C. Jau, C.-T. Hou, I.-C. Khoo, "Single crystal growing of 3D blue-phase photonic crystal (invited paper)," SPIE Optics + Photonics, San Diego, USA, Aug. 30–Sep. 1, 2016.

[3] T.-H. Lin, I.-C. Khoo, T. J. Bunning, and C.-W. Chen, "Single crystal blue-phase photonic crystal (Keynote Presentation)," SPIE Optics + Photonics, San Diego, USA, Aug. 6–10, 2017.